Journal of Energy Chemistry 119 (2026) 53–63

Contents lists available at ScienceDirect

Journal of Energy Chemistry

journal homepage: www.elsevier.com/locate/jechem

http://www.journals.elsevier.com/journal-of-energy-chemistry/

Stabilizing active cobalt sites by interstitial carbon and nitrogen co-doping in metallic cobalt for efficient alkaline oxygen evolution reaction

Jingmei Min[a,1], Hao Li[a,b,1], Xueyan Wu[a], Yan Lv[a], Xingyun Li[a], Jixi Guo[a,*], Artem R. Oganov[c,*], Dianzeng Jia[a,*]

[a] State Key Laboratory of Chemistry and Utilization of Carbon Based Energy Resources, College of Chemistry, Xinjiang University, Urumqi 830017, Xinjiang, China
[b] Institute of Medical Engineering Interdisciplinary Research, College of Medical Engineering and Technology, Xinjiang Medical University, Urumqi 830017, Xinjiang, China
[c] Skolkovo Institute of Science and Technology, 30-1 Bolshoy blvd, Moscow 121205, Russia

ARTICLE INFO

Article history:
Received 3 March 2026
Revised 14 April 2026
Accepted 20 April 2026
Available online 5 May 2026

Keywords:
Co-based catalysts
Co-doping
Interstitial solid solution
Oxygen evolution reaction

ABSTRACT

Cobalt (Co)-based catalysts have emerged as one of the most promising alternatives to ruthenium-based materials for oxygen evolution reaction (OER). However, they suffer from dissolution of cobalt active sites during OER operation, which leads to structural degradation and deactivation of catalytic centers. Here, we present a carbon (C) and nitrogen (N) co-doping strategy to construct a novel Co/Co_4(C,N) electrocatalyst, in which the interstitial C-N solid solution can effectively stabilize the Co active sites through metal–C/N bonding interactions, enabling efficient and durable OER in alkaline media. The Co/Co_4(C,N) catalyst exhibits exceptional OER performance, achieving an overpotential of only 203 mV at 10 mA cm^{-2} and maintaining stability for 300 h, outperforming the benchmark RuO_2. Ab initio molecular dynamics (AIMD) simulations reveal that the interstitial C-N solid solution structure effectively increases the dissolution energy of Co sites, thereby improving the structural stability of the catalysts. X-ray absorption spectroscopy, in situ spectroscopy, and theoretical calculations reveal that the incorporation of interstitial C and N atoms effectively regulates the electronic structure of Co sites and strengthens the adsorption of OER intermediates, which further anchors Co active centers and enhances the catalytic stability. This work provides critical insights into stabilizing metal centers through a co-doping strategy to develop highly active and durable electrocatalysts for energy conversion.

1. Introduction

Exploring efficient oxygen evolution reaction (OER) electrocatalysts is crucial for advancing renewable energy conversion technologies [1–5]. However, the OER occurring at the anode involves the transfer process of four electrons with sluggish kinetics, which limits the overall efficiency of electrochemical water splitting [6–9]. Currently, Ru-based precious metal materials are widely considered as benchmark OER electrocatalysts due to their exceptional intrinsic activity, yet their practical application is severely hindered by high cost and poor stability [10,11]. Therefore, the rational design and development of advanced electrocatalysts is crucial for achieving sustainable OER applications.

Cobalt (Co)-based catalysts, such as oxides, phosphides, nitrides, carbides, and fluorides, have attracted significant attention as promising OER alternatives owing to their earth abundance, tunable electronic configurations, and rich structural diversity [12–17]. However, the electrochemical stability of Co-based catalysts is compromised by the leaching and dissolution of metal cations during the OER process [18,19], leading to undesirable structural disintegration and subsequent deactivation of the catalytic centers. Hence, employing effective strategies to stabilize Co active sites under oxidative conditions is essential to achieve durable alkaline OER electrocatalysis. Recent studies suggest that metal doping can modulate the electronic properties of OER catalysts, optimizing the adsorption and desorption of oxygen intermediates while enhancing catalyst durability [20,21]. For instance, Yu et al. reported that Mn doping into the $LaCoO_3$ to form perovskite oxide $LaCo_{1-x}Mn_xO_3$

---

* Corresponding authors.

E-mail addresses: jxguo1012@163.com (J. Guo), a.oganov@skoltech.ru (A.R. Oganov), jdz@xju.edu.cn (D. Jia).

[1] These authors contributed equally to this work.

https://doi.org/10.1016/j.jechem.2026.04.058
2095-4956/

achieves a dynamic dissolution-deposition equilibrium of cobalt species. The self-catalysis of Mn promotes the redeposition of leached Co as CoO_2, which ensures the long-term stability [22]. Li et al. demonstrated that doping Ru single atoms into cobalt nitride lattices facilitates surface reconstruction and suppresses irreversible cobalt dissolution under OER conditions [23]. Beyond metal doping, non-metallic elements with high electronegativity (such as B, C, N, F, and P) have also been introduced into transition metal lattices to enhance the hybridization of *d-p* orbitals and strengthen the bonding interactions, thereby tuning the adsorption strength and stabilizing the catalytic sites [24–29]. For example, Ji et al. found that fluorine doping into the $CoFe_2O_4$ electrocatalyst induced charge redistribution and accelerated CoOOH formation, improving the reaction kinetics and catalytic activity of OER [27]. Furthermore, simultaneous doping of multiple elements can leverage the synergistic effect of species with distinct electronic configurations to further stabilize metal centers for superior OER efficiency [30–32]. For instance, Huang et al. co-incorporated N and P dopants into MoS_2 nanorods, which occupy partial S-vacancies and trigger phase transformation, regulating the electronic structure and *d*-band center of MoS_2@NPC and enabling enhanced OER performance [28]. Therefore, adopting the co-doping approach represents a promising strategy can effectively modify the electronic structure of the anchored metal centers and modulate the adsorption strength of the intermediates, ultimately enhancing both the electrocatalytic performance and stability under harsh operating conditions.

In this work, we report a carbon (C) and nitrogen (N) co-doping strategy to fabricate a novel Co/Co_4(C,N) electrocatalyst, comprising metallic cobalt and interstitial C-N solid solution with metal–C/N bonding interactions, for efficient alkaline OER. Specifically, the C and N co doping was performed via chemical vapor deposition (CVD) using melamine as the carbon and nitrogen source. The Co/Co_4(C,N) catalyst exhibits exceptional OER activity with an overpotential of only 203 mV to reach 10 mA cm^{-2} and maintains stable operation for 300 h, outperforming most reported Co-based catalysts as well as the state-of-the-art RuO_2. Ab initio molecular dynamics (AIMD) simulations demonstrate that the interstitial solid solution structure increases the dissolution energy of Co sites, thereby imparting enhanced stability. The incorporation of interstitial C and N atoms effectively modulates the electronic structure of Co centers, as evidenced by X-ray absorption spectroscopy, in situ spectroscopy, and theoretical calculations, leading to strengthened adsorption of OER intermediates. Specifically, integrated crystal orbital Hamilton population (ICOHP) and *d*-band center analyses indicate that the interstitial atoms bolster the binding strength between active Co atoms and adsorbed oxygen intermediates, which immobilizes surface Co sites and thus improves catalytic stability. This work innovatively explored the interstitial solid-solution structure to stabilize cobalt active sites during OER electrolysis, offering crucial insights into the design of future catalysts for water electrolysis.

2. Experimental

2.1. Materials

Cobalt (II) chloride hexahydrate ($CoCl_2·6H_2O$, ≥98.0%), ammonium fluoride (NH_4F, ≥98.0%), urea (CH_4N_2O, ≥99.5%), melamine ($C_3N_6H_6$, 99%), and potassium hydroxide (KOH, 95%) were purchased from Energy Chemical. Nafion solution (5 wt%) and ruthenium (IV) oxide (RuO_2, 99.9%) were purchased from Sigma-Aldrich. Carbon cloth (CC) was purchased from Taiwan Carbon Technology Co., Ltd. CC substrates were typically cleaned by sequential ultrasonication in 3 M HCl solution, deionized water, and ethanol for 30 min each to eliminate impurities. All the chemicals were directly used as received without any further purification.

2.2. Sample preparation

2.2.1. Synthesis of Co-based precursors

The Co-based precursor $Co(CO_3)_{0.5}OH$ (denoted as CoCH) on CC was synthesized via a simple hydrothermal method. First, 1 mmol of $CoCl_2·6H_2O$, 2 mmol of NH_4F, and 5 mmol of CH_4N_2O were dissolved into 15 mL of deionized water and ultrasonicated for 30 min to obtain a well-dispersed solution. The above mixed solution was then transferred to a 25 mL Teflon-lined stainless-steel autoclave containing a clean CC substrate (2 cm×3 cm). Subsequently, the sealed autoclave was heated at 120 °C for 6 h to facilitate in situ growth of the CoCH precursor on the CC substrate. After the reaction, the obtained CoCH/CC precursor was sequentially rinsed several times with deionized water and subsequently dried at 60 °C.

2.2.2. Synthesis of interstitial solid solution Co/Co_4(C,N)

The interstitial solid solution Co/Co_4(C,N) was prepared via the CVD method. Specifically, 1.5 g of $C_3H_6N_6$ and the CoCH/CC precursor were placed at the upstream and center in a tubular furnace, respectively. Then, the tube furnace was heated to 800 °C for 5 h with a ramping rate of 5 °C min^{-1} under the N_2 atmosphere to obtain Co/Co_4(C,N). Moreover, the loading amount of as-prepared Co/Co_4(C,N) on CC catalyst was ~1.7 mg cm^{-2}. For comparison, the Co/Co_4(C,N)-8h sample was synthesized using the same procedure, except that the heat treatment time was increased to 8 h.

2.2.3. Synthesis of RuO_2 electrode

Commercial RuO_2 powder (5 mg) was dispersed in 1 mL of a mixture containing 980 μL of ethanol and 20 μL of Nafion solution (5 wt%). After ultrasound for at least 30 min, a homogeneous catalyst ink was achieved. Then, 240 μL of the ink was uniformly dripped onto CC substrate with a size of 0.35 cm^2, resulting in a catalyst loading of 1.7 mg cm^{-2}.

3. Results and discussion

3.1. The design of interstitial C-N solid solution

The structural design pathway for interstitial C-N solid solution Co_4(C,N) is illustrated in Fig. 1(a). The α-Co with the $Fm\bar{3}m$ space group features large [Co_6] octahedral interstices, which are sufficiently spacious to accommodate a N or C atom, forming [NCo_6] or [CCo_6] octahedra. According to the Hagg's rule [33,34], carbon atom has an atomic radius similar to that of nitrogen (R_C = 0.77 Å, R_N = 0.74 Å). Moreover, the radius ratios of both C and N to the Co atom (R_C/R_{Co} = 0.616, R_N/R_{Co} = 0.600) slightly exceed the critical threshold of 0.59. Consequently, only one of the four octahedral interstitial sites in the α-Co lattice is occupied by a C or N atom, forming the cubic antiperovskite structure with the C or N atom located at the body center, thereby resulting in the chemical formulas Co_4C or Co_4N and a reduction in symmetry to the $Pm\bar{3}m$ space group.

Then, the geometry optimization of Co_4C and Co_4N were first performed using density functional theory (DFT) calculations, and the lattice geometry was fully relaxed with respect to both the unit cell and atomic positions. The resulting optimized structures with lattice constants found that the two phases exhibit nearly identical lattice constants of $a_{(Co_4C)}$ = 3.73 Å and $a_{(Co_4N)}$ = 3.72 Å, indicating that the two compounds are capable of forming a continuous solid solution Co_4(C,N). As the parent phases of this continuous solid solution, Co_4N is a known compound, whereas Co_4C remains experimentally unreported. Herein, we conducted crystal structure

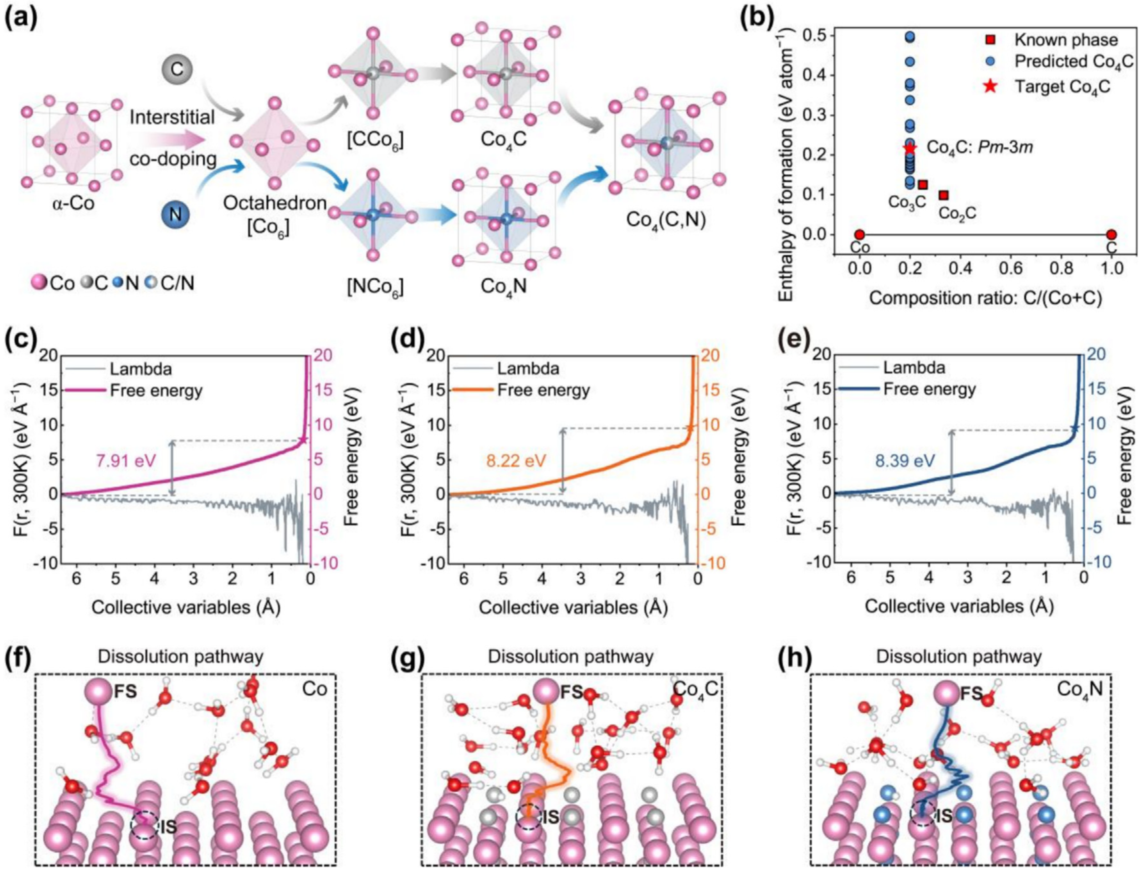

Fig. 1. (a) Schematic illustration of the design of interstitial C-N solid solution $Co_4(C,N)$. (b) Convex hull diagram for the Co-C binary system. Dissolution energy for surface Co atoms for (c) Co, (d) Co_4C, and (e) Co_4N using the slow-growth approach, and (f–h) the corresponding structural models and the schematic diagram of the dissolution pathways.

prediction (CSP) using USPEX to evaluate the Co_4C phase. Initially, fixed-composition CSP was performed for Co_4C at a Co:C ratio of 4:1, which resulted in 24 distinct predicted structures. Fig. 1(b) presents the obtained convex hull of the Co–C system to evaluate thermodynamic stability. The compounds located at the convex hull have formation enthalpies equal to zero, implying that they are thermodynamically stable. In contrast, the compounds positioned above the convex hull are thermodynamically metastable, with their formation enthalpies corresponding to the vertical distance from the convex hull. The red square markers represent the reported Co-C binary compounds, among which only two cobalt carbide phases, Co_2C and Co_3C, have been found thus far. Based on the CSP results, the lowest-energy phase of Co_4C is predicted to be about 0.13 eV atom^{-1} above the convex hull, while the targeted $Pm\bar{3}m$ structure lies over 0.22 eV atom^{-1} in energy. The high formation enthalpy of cobalt carbide signifies its metastable nature, posing a significant thermodynamic challenge for the synthesis of bulk Co_4C. Nevertheless, such metastable compounds could be stabilized on appropriate surfaces. Yue et al. reported the copper boride formed on Cu crystal surfaces despite the absence of bulk copper boride phases [35]. This result revealed the feasibility of experimentally synthesizing cobalt carbide on the Co surfaces.

To evaluate the stability of surface Co sites after introducing interstitial atoms in a pure water environment, we performed constrained AIMD simulations on the parent phases (Co, Co_4C, and Co_4N) using the slow-growth approach with an explicit solvent model. The resulting dissolution energy profiles along the reaction path for Co, Co_4C, and Co_4N were used to simulate the dynamic process and free energy of surface Co atoms dissolved into water. A higher dissolution energy value signifies that the Co atoms are less prone to detach from the surface, implying a lower dissolution tendency and higher stability. As illustrated in Fig. 1(c–e), the Co_4C (8.22 eV) and Co_4N (8.39 eV) exhibit more positive dissolution energy of surface Co atoms than the Co (7.91 eV); the higher dissolution energy suggests that the surface Co atoms in Co_4C and Co_4N are more difficult to dissolve out. Moreover, the structural configurations of the initial state (IS) and final state (FS), along with the corresponding dissolution pathways of Co atoms for Co, Co_4C, and Co_4N, are presented in Fig. 1(f–h). Based on the above analysis of kinetic stability in aqueous environments, interstitial C-N solid solution $Co_4(C,N)$ demonstrates enhanced stability relative to metallic Co and thus emerges as a potential alternative.

3.2. Synthesis and structural characterizations

The interstitial solid solution $Co/Co_4(C,N)$ catalyst supported on conductive CC was synthesized through a two-step process (Fig. 2a). First, cobalt-based CoCH nanowire precursors were grown hydrothermally on the CC substrate (Figs. S1–S4). Then, C and N co doping was performed via the CVD method under an inert atmosphere, where melamine served as both the carbon and nitrogen source, to obtain the final interstitial solid solution $Co/Co_4(C,N)$ catalyst. The crystallographic structure of the interstitial solid solution $Co/Co_4(C,N)$ was characterized by X-ray diffraction (XRD) with a scan step of 0.01°, as depicted in Fig. 2(b). The weak diffraction peaks observed at 44.12° and 51.46° correspond to the (111) and (200) facets of the cubic phase metallic Co (PDF#01-089-7093).

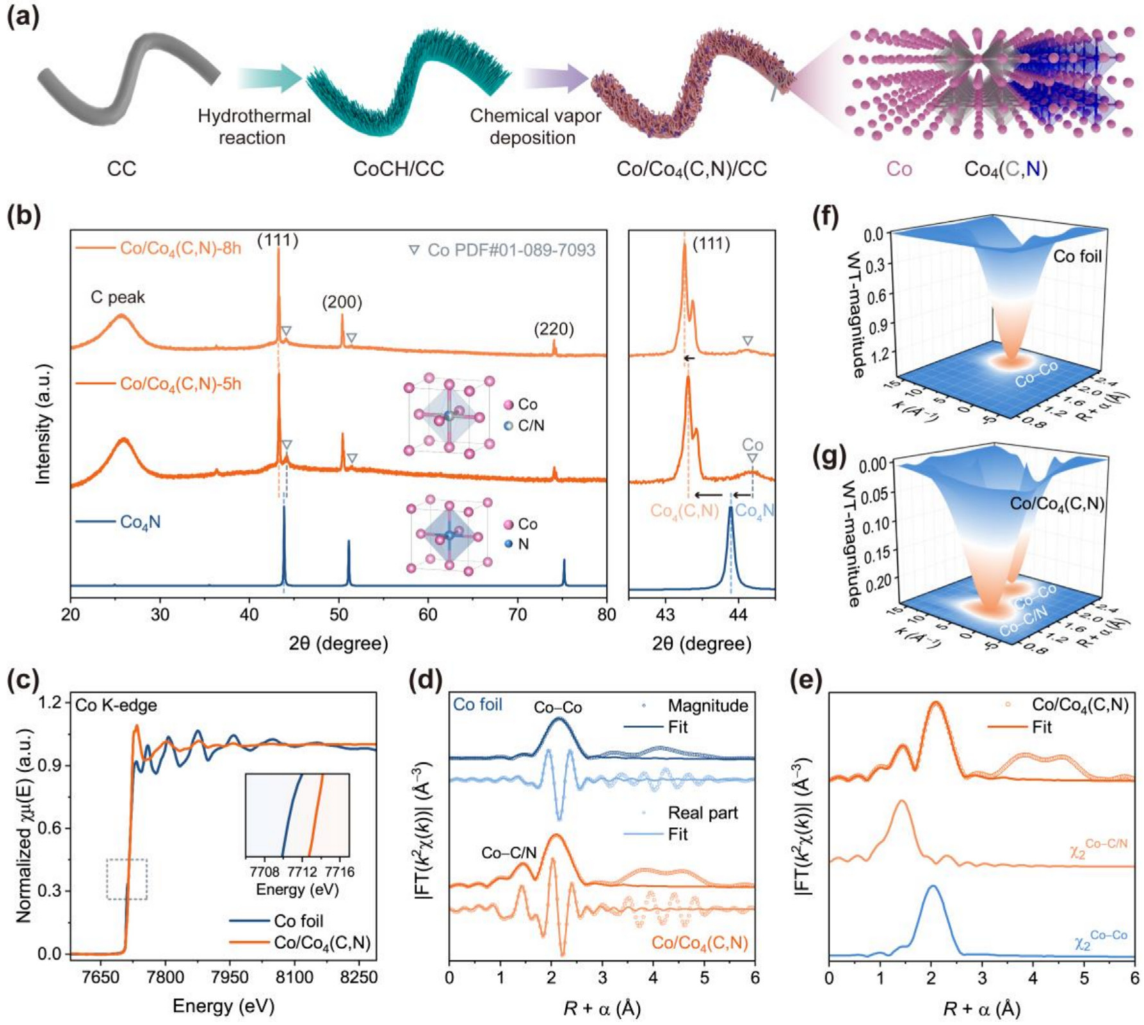

Fig. 2. (a) Schematic illustration of the synthetic process of Co/Co_4(C,N) solid solution catalyst. (b) XRD patterns of Co/Co_4(C,N) and reference Co_4N. Inset: the corresponding crystal structure models. Right: the corresponding local enlargement. (c) Normalized Co *K*-edge XANES spectra of Co foil and Co/Co_4(C,N). The inset shows a local magnified region. (d) FT-EXAFS spectra (circles) and corresponding fitting curves (lines) for Co foil and Co/Co_4(C,N). (e) Co *K*-edge EXAFS fitting analyses for Co/Co_4(C,N). WT-EXAFS contour plots of (f) Co foil and (g) Co/Co_4(C,N).

The standard pattern of the known Co_4N phase (PDF#04-021-6262) was used as a reference [36,37]. The incorporation of interstitial N atoms expands the Co lattice constant from 3.552 Å for α-Co to 3.570 Å for Co_4N, which in turn shifts the corresponding diffraction peak from 44.2° for Co to a lower angle of 43.9° for Co_4N, as clearly seen in the magnified pattern (Fig. 2b, right panel). Notably, it is observed that after doping with C and N, the 2θ peak in the (111) direction of the Co/Co_4(C,N) sample shows a clear shift of 0.6° toward a lower angle compared to that of Co_4N. This shift can be attributed to the entry of interstitial C and N atoms into the Co lattice, resulting in a lattice expansion of the Co framework (Table S1). As the reaction time was increased from 5 to 8 h, the (111) peak of the Co/Co_4(C,N) catalyst slightly shifted to a lower angle from 43.31° to 43.26°, further confirming the successful formation of an interstitial solid solution structure.

X-ray absorption near-edge structure (XANES) and extended X-ray absorption fine structure (EXAFS) spectroscopy were further performed to disclose the coordination environments of Co/Co_4(C,N). As seen in the normalized Co *K*-edge XANES spectra (Fig. 2c), the absorption edge of the Co/Co_4(C,N) shifts to higher energy compared to that of Co foil, which clearly reveals the pronounced electron transfer from Co to C/N atoms. The Fourier-transformed (FT) Co *K*-edge EXAFS spectra of samples in Fig. 2(d) reveal distinct local structures for Co/Co_4(C,N). The prominent peak at 1.45 Å is attributed to the Co–C/N first coordination shell, while the peak at 2.11 Å corresponds to a Co–Co scattering path, suggesting the presence of metallic cobalt and an interstitial C-N solid solution Co_4(C,N), consistent with the characteristics observed in the XRD results. In contrast, the Co foil reference exhibits a single coordination peak at a distance of 2.15 Å, corresponding to metallic Co–Co coordination. We have fitted the coordination environment of Co atom in Co foil and Co/Co_4(C,N) to analyze the structural differences in more detail, and the fitting results are shown in Fig. 2(e) and Table S2, in agreement with the experimental spectra. The Co atoms in Co/Co_4(C,N) have two coordination structures of Co–Co and Co–C/N, with the Co–C/N bond length of 1.92 Å with coordination number (CN) of 2.7. Meanwhile, the Co–Co bond length of 2.44 Å with CN of 8.8 proves the presence of Co/Co_4(C, N) solid solution. In addition, the coordination environment can be further visualized by the corresponding wavelet transform (WT) analysis. The WT contour plot of Co/Co_4(C,N) presents a dominant intensity maximum signal at 4.12 $Å^{-1}$, attributed to Co–C/N coordination, along with a weaker feature at 6.92 $Å^{-1}$ indicative of Co–Co bonding. These findings confirm that Co species are primarily in the form of Co–C/N and Co–Co bonds, which is distinctly different from the reference Co foil (Fig. 2f, g). Therefore, the above results confirm the successful synthesis of interstitial solid solution $Co/Co_4(C,N)$ composite.

3.3. Composition and morphological characterizations

X-ray photoelectron spectroscopy (XPS) was conducted to probe the surface compositions and chemical states of interstitial solid solution $Co/Co_4(C,N)$. The survey spectrum confirms the presence of Co, C, N, and O signals in $Co/Co_4(C,N)$ (Fig. S5). As displayed in Fig. 3(a), the high-resolution Co 2*p* spectra of $Co/Co_4(C,N)$ features two main peaks corresponding to the Co $2p_{3/2}$ and Co $2p_{1/2}$ spin-orbit doublets, along with their shake-up satellite peaks. Specifically, the dominant peaks at 779.6 and 795.4 eV are assigned to metallic Co (Co^0), while the peaks at 781.7 and 797.2 eV and the peaks at 785.4 and 802.1 eV were ascribed to the Co–C/N bond and satellite peaks, respectively. Meanwhile, the C 1*s* spectrum of $Co/Co_4(C,N)$ can be deconvolved to the characteristic peaks of Co–C (283.5 eV), C–C (284.8 eV), C–N (287.2 eV), and O–C=O bonds (290.9 eV) (Fig. 3b). Additionally, Fig. 3(c) shows the spectrum of N 1*s* with three peaks corresponding to the Co–N (397.4 eV) [38], N–H (399.4 eV) [39], and N–O (402.1 eV) bonds for $Co/Co_4(C,N)$. Fig. S6 exhibits the O 1*s* spectra of $Co/Co_4(C,N)$. The binding energies at 530.2 and 531.1 eV were assigned to lattice oxygen (O_L) and oxygen vacancies (O_v), respectively. Raman analysis further confirms the characteristic peaks detected at 183, 457, 497, and 657 cm^{-1} in the spectrum of $Co/Co_4(C,N)$ (Fig. 3d). In addition, the scanning electron microscopy (SEM) image shows that interstitial solid solution $Co/Co_4(C,N)$ displays carbon nanotubes (CNTs) morphology, in which the in situ grown CNTs intertwine to form a three-dimensional interconnected conductive network (Fig. 3e). Subsequently, high-resolution transmission electron microscopy (HRTEM) images further verify its nanotubular morphology and the crystal structure of solid solution $Co/Co_4(C,N)$ (Fig. 3f, g). The spacings of lattice fringes are measured to be 0.208 and 0.145 nm, corresponding to the (1 1 1) and (211) crystal planes of $Co/Co_4(C,N)$, respectively, indicating the in situ formation of interstitial solid solution $Co/Co_4(C,N)$. The corresponding fast Fourier transform (FFT) analysis (inset of Fig. 3g) exhibits two diffraction spots of (111) and (211) planes oriented along the $[01\bar{1}]$ zone axis. Meanwhile, Fig. 3(h and i) presents the inverse FFT (IFFT) pattern from the Fig. 3(g), and the corresponding intensity profile analysis can be seen in Fig. 3(j). Energy-dispersive X-ray spectroscopy (EDS) mappings and the corresponding spectrum (Figs. S7 and S8) further indicate the uniform distribution of Co, C, N, and O elements in interstitial solid solution $Co/Co_4(C,N)$ (Fig. 3k). Inductively coupled plasma-optical emission spectroscopy (ICP-OES) analysis revealed that the Co content in solid solution $Co/Co_4(C,N)$ was 3.25 wt% (Table S3).

3.4. Electrocatalytic performance for alkaline OER

The OER performance of $Co/Co_4(C,N)$ was evaluated in the O_2-saturated 1.0 M KOH electrolyte by employing a conventional three-electrode setup. Before the measurements, the reference electrode was calibrated relative to the reversible hydrogen electrode (RHE) (Fig. S9). As shown in Fig. 4(a), the linear sweep voltammetry (LSV) curves at a current density of 10 mA cm^{-2} show that the overpotential of $Co/Co_4(C,N)$ catalyst was only 203 mV, much lower than that of CoCH (380 mV), commercial RuO_2 (denoted as Com. RuO_2) (316 mV), and blank CC (651 mV). In addition, the $Co/Co_4(C,N)$ exhibited the lowest Tafel slope of 74.9 mV dec^{-1} compared to the control samples, including Com. RuO_2 (81.3 mV dec^{-1}) and CoCH (102.6 mV dec^{-1}), indicating more favorable kinetics in the OER process (Fig. 4b). Meanwhile, the overpotentials of the studied samples at 10 and 100 mA cm^{-2}, along with the Tafel slopes, were presented in a bar chart, revealing its superior OER activity for $Co/Co_4(C,N)$ (Fig. 4c, Fig. S10). The kinetics of electrocatalytic reactions is primarily governed by interfacial charge transfer between electrocatalysts and adsorbates. The charge-transfer resistances (R_{ct}) of the catalysts were obtained from the electrochemical impedance spectroscopy (EIS). As shown in Fig. 4(d), the $Co/Co_4(C,N)$ displayed the smallest R_{ct} of 5.22 Ω compared to CoCH (50.04 Ω) and Com. RuO_2 (28.76 Ω), indicating the fastest reaction kinetics. Cyclic voltammetry (CV) measurements (Figs. S11–S13) were employed to assess the electrochemically active surface areas (ECSA) of the electrocatalysts, derived from their electrochemical double-layer capacitance (C_{dl}). Notably, $Co/Co_4(C,N)$ exhibited the largest C_{dl} value of 26.9 mF cm^{-2}, which was higher than that of the controls including Com. RuO_2 (17.8 mF cm^{-2}) and blank CC (1.1 mF cm^{-2}) (Fig. 4e), suggesting a significant increase in the number of active sites. To assess specific catalytic activities, the current density at 1.53 V vs. RHE was normalized by the ECSA of $Co/Co_4(C,N)$ and Com. RuO_2 catalysts. The results reveal that the value for $Co/Co_4(C,N)$ (0.056 mA cm^{-2}) is approximately 3.73 times higher than that of Com. RuO_2 (0.015 mA cm^{-2}), emphasizing the superior intrinsic catalytic activity of $Co/Co_4(C,N)$ (Fig. 4f). Furthermore, the stability of the $Co/Co_4(C,N)$ catalyst in OER was evaluated using a chronopotentiometry test. As shown in Fig. 4(g), the co-doped $Co/Co_4(C,N)$ catalyst maintained stable operation for 300 h at 10 mA cm^{-2} with no obvious activity degradation. In sharp contrast, the undoped Co sample and Com. RuO_2 suffered from a rapid potential increase within just 30 h. This difference highlights that the co-doping of interstitial C and N plays an important role in inhibiting Co dissolution and enhancing catalytic stability under alkaline OER conditions. To further investigate the structural and chemical stability of $Co/Co_4(C,N)$ catalyst, XRD, HRTEM, and XPS characterizations were conducted after the OER tests. No significant crystal structure transformation of the $Co/Co_4(C,N)$ was observed, as shown by the XRD in Fig. S14, indicating that the structure of $Co/Co_4(C,N)$ catalyst was maintained. The XPS analysis for the catalyst, specifically the binding energy of Co 2*p* for $Co/Co_4(C,N)$ after the stability test, exhibited a slight shift toward higher binding energy values (Figs. S15, S16), suggesting partial oxidation of Co sites. Meanwhile, the HRTEM images revealed that the nanotubular morphology of the $Co/Co_4(C,N)$ catalyst after the OER remains unchanged (Fig. S17a). Notably, the lattice fringe corresponding to the (111) plane of the $Co/Co_4(C,N)$ was still visible in the HRTEM images after the OER test (Fig. S17b). To investigate the composition change of the $Co/Co_4(C,N)$ electrode during the stability test, the metal ion dissolution in the electrolyte during OER electrolysis was monitored using inductively coupled plasma mass spectrometry (ICP-MS). Fig. S18 shows that the Co ions leached out of the $Co/Co_4(C,N)$ catalyst rapidly during the initial 2.5 h of the reaction, and the concentration of dissolved Co ions remained essentially stable during the subsequent prolonged OER reaction, with no obvious increase observed thereafter. These results demonstrate that the $Co/Co_4(C,N)$ electrocatalyst possesses excellent chemical and structural stability during long-term OER tests. In addition, a comparison of the other reported Co-based counterparts is shown in Fig. 4(h) (Table S4), further confirming the outstanding catalytic behavior of $Co/Co_4(C,N)$.

3.5. Electrocatalytic mechanism analysis

In situ EIS measurements were conducted at different applied potentials to further elucidate the charge transport behavior at the electrode-electrolyte interfaces. The Nyquist plots (Figs. S19 and S20) and the fitted equivalent circuit parameters (Table S5) show that the R_{ct} values of $Co/Co_4(C,N)$ are much smaller than those of CoCH at all applied potentials tested, confirming its faster

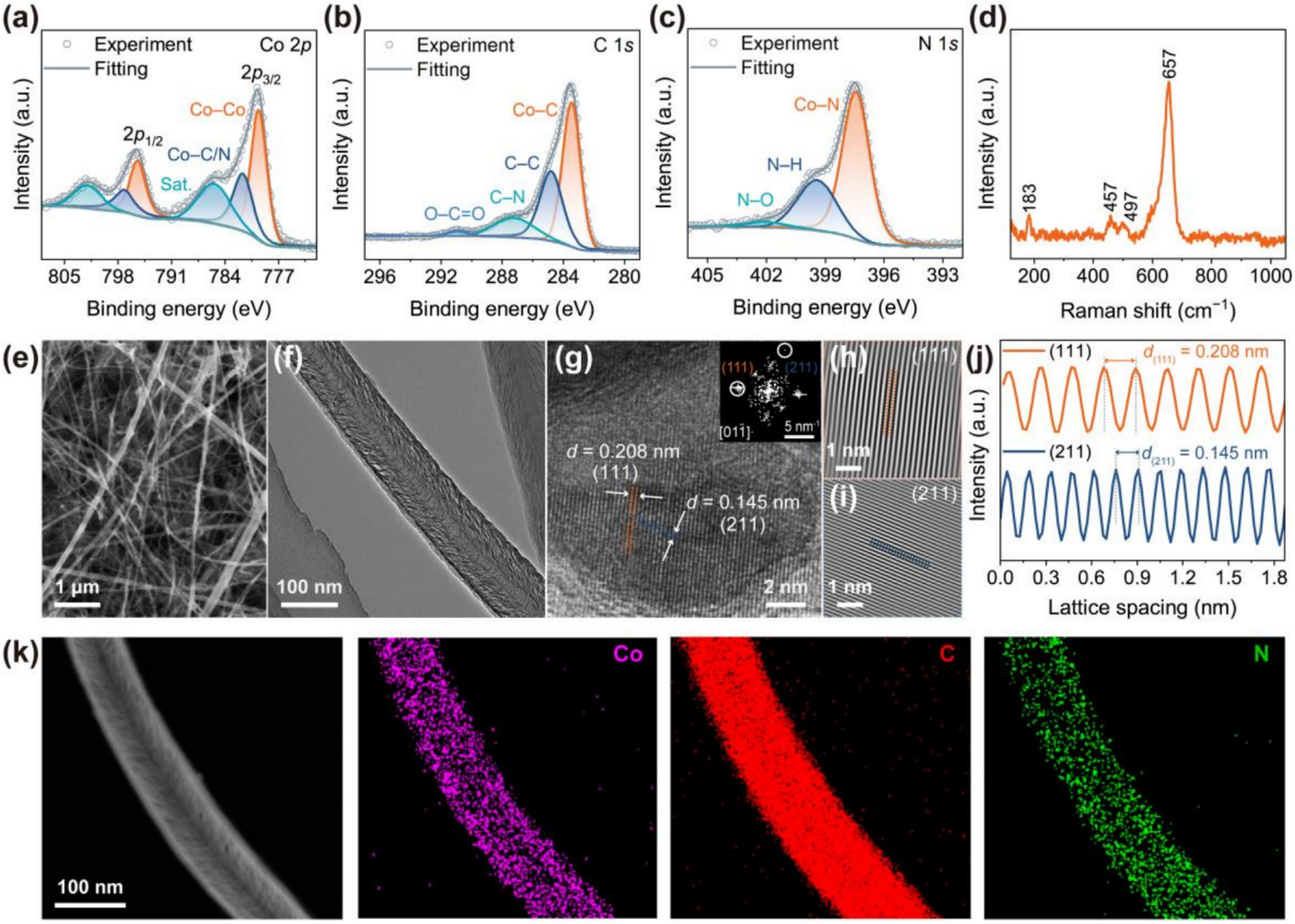

Fig. 3. High-resolution XPS spectra of (a) Co 2*p*, (b) C 1*s*, and (c) N 1*s* for Co/Co_4(C,N). (d) Raman spectra of Co/Co_4(C,N). (e) SEM image of Co/Co_4(C,N). (f, g) HRTEM images of Co/Co_4(C,N) and the corresponding FFT pattern shown in the inset. (h, i) The IFFT patterns and (j) the corresponding intensity profile analysis. (k) EDS mappings of the Co/Co_4(C,N).

reaction kinetics during the alkaline OER process. In the Bode phase plots, the electron transfer response within the catalyst occurs in the high-frequency region of 10^2–10^4 Hz, while the charge transfer response at the catalyst-electrolyte interface is observed in the low-frequency region of 10^{-2}–10^2 Hz [40,41]. As shown in Fig. 5(a and b), Co/Co_4(C,N) displays relatively smaller phase angles in the low-frequency region of the Bode plots compared with CoCH, with these peaks decreasing more rapidly as the potential increases, further suggesting accelerated charge transfer capability at the Co/Co_4(C,N) interface and enhanced OER rate.

To elucidate the OER catalytic mechanism of Co/Co_4(C,N), the pH dependence of Co/Co_4(C,N) was investigated in KOH electrolyte with different pH values (Fig. 5c) [42,43], which exhibited strong pH-dependent activity. As shown in Fig. 5(c) (top panel), the OER activity of Co/Co_4(C,N) markedly decreases upon tetramethylammonium cation (TMA^+) addition, indicating the strong binding between TMA^+ and negatively charged oxygen species generated during the OER catalytic process. Combined with the pH-dependent results, these findings confirm that the OER on Co/Co_4(C,N) primarily follows the lattice oxygen oxidation mechanism (LOM) [44]. Furthermore, the surface coverage of the key OER intermediate, OH^*, was assessed via competitive methanol oxidation reaction (MOR) experiments [45,46]. Methanol molecules prefer to nucleophilically attack the electrophilic OH; therefore, MOR can be applied to detect OH^* coverage. We then applied a methanol molecular probe to measure the OH^* coverage on Co/Co_4(C,N) catalyst. As shown in Fig. 5(c) (bottom panel), Co/Co_4(C,N) exhibits a more pronounced MOR current density enhancement, suggesting stronger OH^* adsorption and higher OH^* coverage on Co/Co_4(C,N) catalyst to motivate OER.

Furthermore, in situ ^{18}O isotope-labeling differential electrochemical mass spectrometry (DEMS) measurement was performed to provide direct evidence for the lattice oxygen-participated LOM pathway in OER. The Co/Co_4(C,N) catalyst was first subjected to LSV measurements for electrochemical pretreatment in 1.0 M KOH electrolyte with $H_2^{18}O$ as the solvent to label ^{18}O onto the surface of catalysts. If the LOM governs the OER, ^{18}O would be incorporated into and exchanged with oxygen atoms in the lattice structure of the catalyst during this pretreatment. Subsequently, the ^{18}O-labeled catalyst was transferred to an $H_2^{16}O$ solution for further LSV measurements, while DEMS continuously monitored the gaseous products. The DEMS results (Fig. 5d) revealed that pronounced periodic signals at $m/z = 32$, $m/z = 34$, and $m/z = 36$ were detected during the OER process for Co/Co_4(C,N), suggesting the presence of $^{32}O_2$ ($^{16}O^{16}O$), $^{34}O_2$ ($^{16}O^{18}O$), and $^{36}O_2$ ($^{18}O^{18}O$) in the products. This result unambiguously implies the engagement of lattice oxygen during OER for Co/Co_4(C,N), confirming that the LOM is the main OER pathway [42,47,48]. Specifically, the amount of $^{34}O_2$ evolved for Co/Co_4(C,N), reflecting the participation of lattice oxygen ($^{34}O_2$ originates from the combination of ^{18}O in the lattice and ^{16}O in the water), is around 2.91%, which is

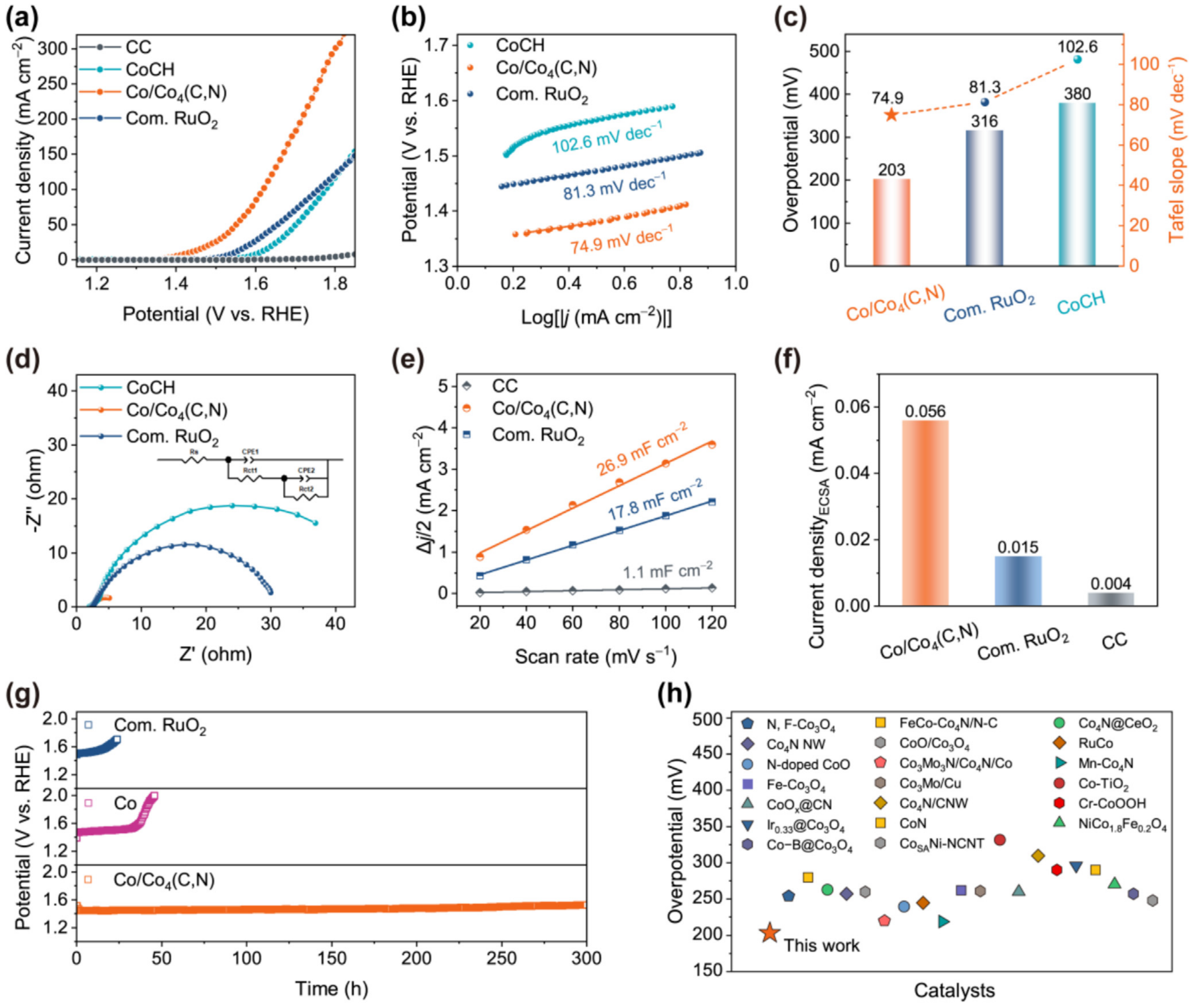

Fig. 4. (a) LSV curves, (b) Tafel slopes, and (c) Bar charts of overpotentials at 10 mA cm^{-2} and Tafel slopes. (d) EIS Nyquist plots. Inset: equivalent circuit model. (e) C_{dl} plots. (f) ECSA-normalized current density values of Co/Co$_4$(C,N), Com. RuO$_2$, and CC at 1.53 V vs. RHE. (g) Chronopotentiometry stability tests of Co/Co$_4$(C,N), Co, and Com. RuO$_2$. (h) Comparison of alkaline OER activity with other reported Co-based electrocatalysts.

significantly higher than the natural isotopic abundance of ^{18}O in water (≤0.2%) [49]. This evidence further confirms that lattice oxygen in Co/Co$_4$(C,N) directly participates in the OER process.

We further carried out in situ attenuated total reflection-surface enhanced infrared absorption spectroscopy (ATR-SEIRAS) on the Co/Co$_4$(C,N) catalyst to monitor the reaction intermediates during the OER. As illustrated in Fig. 5(e), no obvious peaks were found at the open circuit potential (OCP). Upon applying anodic potentials, a relatively weak peak appeared at 1650 cm^{-1}, corresponding to the H–O–H bending vibration of water molecules [50]. Meanwhile, two pronounced absorption peaks appeared at around 1084 and 1230 cm^{-1}, and their intensities increased with increasing applied potential. These peaks can be assigned to the emergence of the O–O stretching of surface-adsorbed OO* intermediates during the OER [51,52], further supporting the conclusion that Co/Co$_4$(C,N) follows the LOM pathway. This result provides direct evidence for the involvement of lattice oxygen of the OER for Co/Co$_4$(C,N), which is well consistent with the findings from DEMS measurements.

3.6. Theoretical insights into the OER mechanism

The Co/Co$_4$(C,N) catalyst compositionally comprises two phases, namely metallic α-Co and interstitial C-N solid solution Co$_4$(C,N). Moreover, Co$_4$C and Co$_4$N (the case of C-only or N-only doping) serve as counterparts maintaining an identical face-centered cubic cobalt skeleton. Therefore, to probe the effects of undoped, C-only, or N-only doped, and co-doped systems, separate slab models of Co, Co$_4$C, Co$_4$N, Co$_4$(C,N), and Co/Co$_4$(C,N) were constructed for theoretical calculations. The (110) surface of these models was built based on the exposed facets identified by HRTEM. DFT calculations were then performed to provide insight into the alkaline OER mechanism. Identifying the most stable surface termination under actual reaction conditions is crucial. During the OER process in an alkaline medium, the pristine surfaces of Co-based catalysts undergo progressive oxidation to form active oxide/oxyhydroxide layers. To determine the actual surface states of the Co, Co$_4$C, Co$_4$N, Co$_4$(C,N), and Co/Co$_4$(C,N) catalysts under OER conditions, we initially constructed surface models covered with one

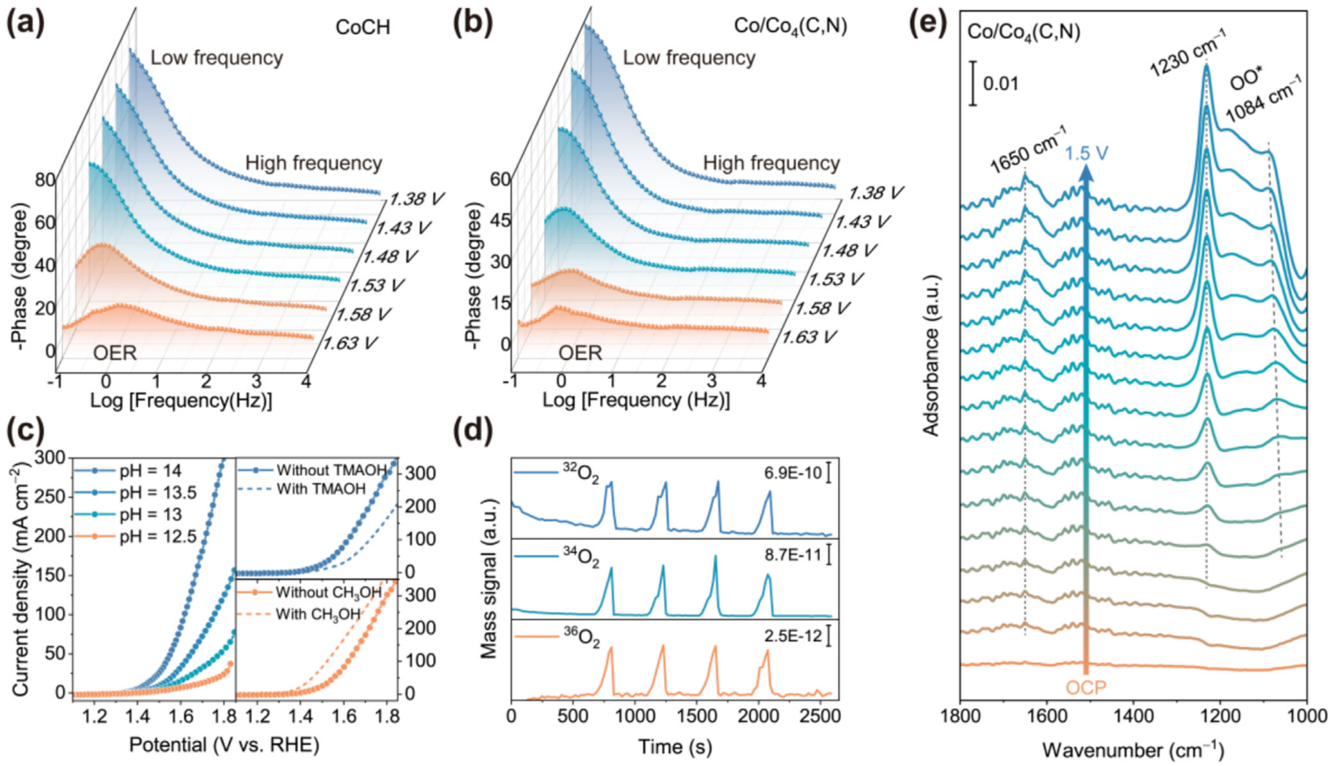

Fig. 5. Bode phase plots of (a) CoCH and (b) Co/Co_4(C,N) for OER at different potentials. (c) Left: LSV curves of Co/Co_4(C,N) in 1.0 M KOH with different pH values. Right: LSV curves of Co/Co_4(C,N) in 1.0 M KOH with and without TMAOH (top) and CH_3OH (bottom), respectively. (d) DEMS signals of $^{32}O_2$, $^{34}O_2$, and $^{36}O_2$ from the gas products for ^{18}O-labeled Co/Co_4(C,N) in 1.0 M KOH with $H_2^{16}O$ as the solvent. (e) In situ ATR-SEIRAS spectra of Co/Co_4(C,N).

monolayer (1 ML) oxygen species (O* and OH*) (Figs. S21–S23). Subsequently, we present the surface Pourbaix diagrams [53] for Co, Co_4C, Co_4N, Co_4(C,N), and Co/Co_4(C,N) (110) facets at the standard hydrogen electrode (U = SHE, pH = 14) in Fig. 6(a–c) and Fig. S24, which exhibit three distinct regions, including pristine, OH, and O terminations. The results clearly indicate that all surfaces are pre-covered with approximately 1 ML O* under OER conditions. The O*-terminated structure was identified as the most stable among all compounds examined in this study. Consequently, we selected the corresponding surface structure with the most stable 1 ML O* coverage for further activity calculations.

The aforementioned experimental results confirmed that lattice oxygen in Co/Co_4(C,N) directly participates in the OER. A complete reaction pathway for the LOM under alkaline OER conditions is provided, as detailed in the schematic diagram of Fig. 6(d), which comprises four distinct electrochemical steps, including O–O coupling, O_2 release, and OH* recovery steps [54]. Moreover, the Gibbs free energy of the OER steps on Co, Co_4C, Co_4N, Co_4(C,N), and Co/Co_4(C,N) through the LOM pathway was calculated, as shown in Fig. 6(e). The optimized structure models with adsorbed oxygen intermediates are detailed in the Figs. S25–S29. Notably, Co exhibits a significantly lower energy barrier (0.676 eV) than Co_4C (0.992 eV), Co_4N (1.339 eV), Co_4(C,N) (1.026 eV), and Co/Co_4(C,N) (0.965 eV) under the equilibrium potential (U = 1.23 V). Meanwhile, we can find that the C and N co-doped Co framework exhibits an energy barrier that lies between those of the C-doped and N-doped counterparts. It is notable that the Co/Co_4(C,N) exhibits a significantly lower kinetic barrier than both singly doped and co-doped phases, which rationalizes the enhanced catalytic performance observed experimentally.

More specifically, the projected crystal orbital Hamilton population (pCOHP) was used to analyze the bonding strength between active metal centers and the oxygen intermediates [55]. The integrated COHP (ICOHP) was calculated to quantify the bonding strength of the active Co sites and adsorbed O intermediates. The higher the absolute values of the ICOHP, the stronger the bonding interactions. As shown in the left panels of Fig. 6(f–h) and Fig. S30, compared with Co (−2.087 eV), the ICOHP values for Co_4C, Co_4(C, N), and Co_4N were determined to be −2.515, −2.518, and −2.521 eV, respectively, indicating a progressive enhancement of the Co–O bonding strength upon the interstitial incorporation of C and N atoms. Meanwhile, Co_4(C,N) shows a moderate Co–O bonding strength with simultaneous C and N doping, which lies between those of Co_4C and Co_4N. Strikingly, Co/Co_4(C,N) achieves a ICOHP value of −2.106 eV, which is slightly stronger than that of Co (−2.087 eV) and significantly weaker than that of the Co_4C, Co_4N, and Co_4(C,N), representing an optimized bonding strength between the Co center and the oxygen intermediate.

Moreover, projected density of states (PDOS) was calculated to investigate the orbital interactions between Co 3d and O 2p states. Generally, the d-band center serves as a key descriptor of the binding strength between the metal active centers and adsorbates. The d-band center closer to the Fermi level (E_f) will induce a stronger binding strength with adsorbates [56]. As shown in the right panels of Fig. 6(f–h) and Fig. S30, the d-band centers of Co_4C (−2.051 eV), Co_4N (−1.933 eV), and Co_4(C,N) (−1.942 eV) are shifted to higher energies compared to that of Co (−2.286 eV), which signifies strengthened adsorption of the O intermediate species after incorporation of C and N atoms. Notably, the d-band center of Co/Co_4(C, N) is shifted to −2.228 eV to achieve a desirable adsorption capacity of O intermediates compared with that of Co (−2.286 eV) and Co_4(C,N) (−1.942 eV), which is beneficial for the OER process and aligns with the COHP results.

The above findings suggest that the primary catalytic activity originates from the metallic Co, the interstitial C-N solid solution Co_4(C,N) reinforces the adsorption strength of OER intermediate

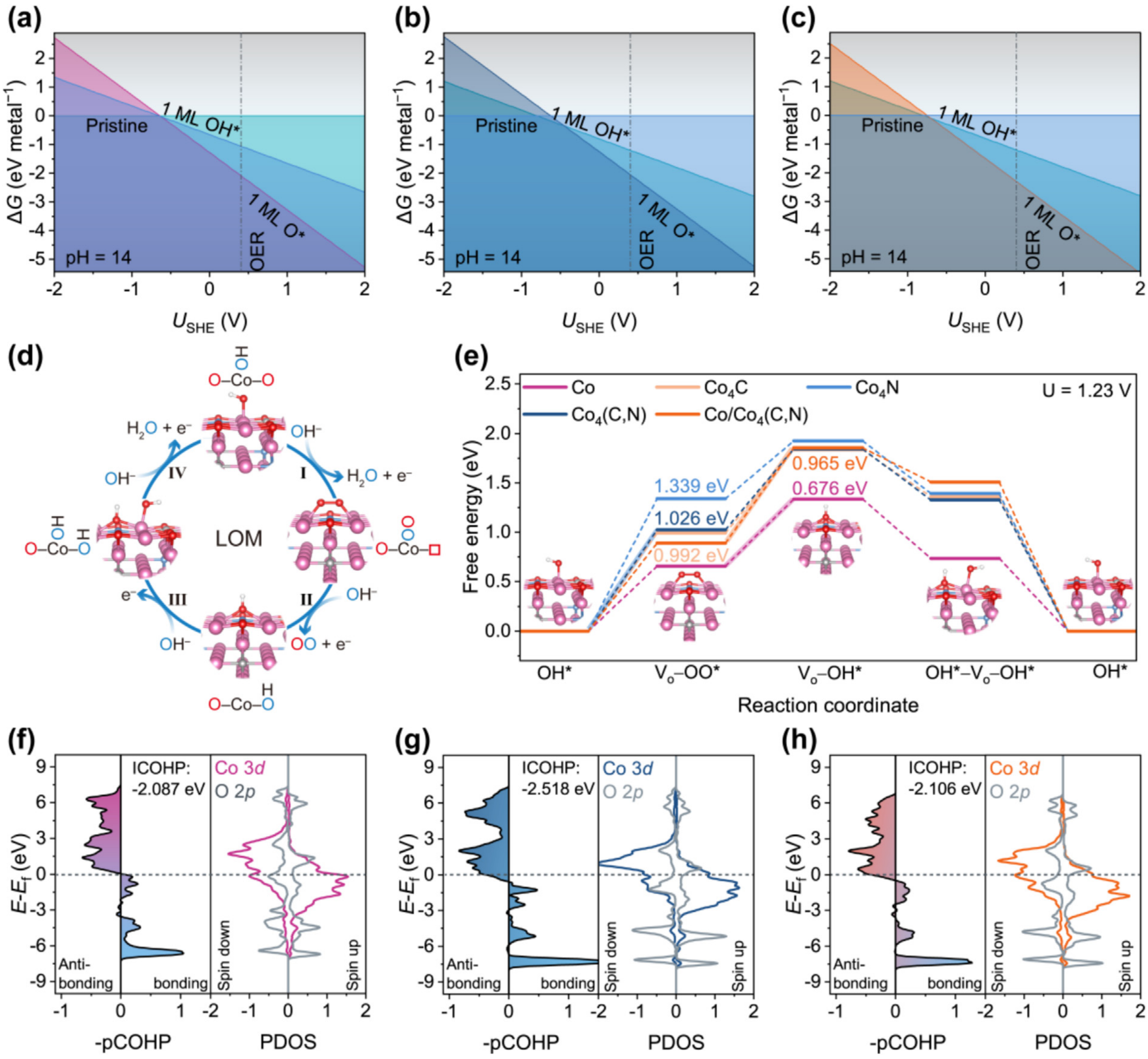

Fig. 6. Calculated surface Pourbaix diagram as a function of potential vs. SHE for (a) Co, (b) Co_4(C,N), and (c) Co/Co_4(C,N). (d) LOM schematic illustration of OER mechanisms. The empty square represents the oxygen vacancy. (e) Gibbs free energy diagrams of the OER process for Co, Co_4C, Co_4N, Co_4(C,N), and Co/Co_4(C,N). The inset shows the schematics of the structural models; the pink, grey, white, and red spheres represent Co, C, H, and O atoms, respectively. The pCOHP (left) and PDOS (right) for the (f) Co, (g) Co_4(C,N), and (h) Co/Co_4(C,N).

species to anchor surface Co atoms. Thus, from the perspective of electronic structure, the optimized OER performance of Co/Co_4(C, N) is attributed to the optimal balance between high electroactivity and stability.

4. Conclusions

In summary, we have successfully constructed a new interstitial solid solution Co/Co_4(C,N) electrocatalyst by co-doping C and N to address the critical issue of Co sites dissolution in Co based OER catalysts. AIMD simulations reveal that the interstitial C-N solid-solution structure can increase the dissolution energy of the Co active center. Moreover, COHP and *d* band center analyses demonstrate that the incorporation of interstitial C and N atoms can effectively modulate the electronic configuration of the Co active center, thereby enhancing the adsorption of OER intermediates and further anchoring Co sites to improve catalyst durability. This work innovatively explores the utilization of an interstitial solid solution for sustaining metal cobalt sites under OER electrolysis and provides crucial insights into future catalyst design for water electrolysis.

CRediT authorship contribution statement

Jingmei Min: Writing – review & editing, Writing – original draft, Visualization, Validation, Methodology, Investigation, Formal analysis, Data curation, Conceptualization. **Hao Li:** Writing – review & editing, Visualization, Validation, Software, Methodology, Investigation, Formal analysis, Data curation, Conceptualization. **Xueyan Wu:** Writing – review & editing, Supervision, Formal analysis. **Yan Lv:** Writing – review & editing, Supervision, Formal analysis. **Xingyun Li:** Writing – review & editing, Supervision, Formal analysis. **Jixi Guo:** Writing – review & editing, Supervision, Resources, Project administration, Methodology, Funding acquisition, Formal analysis, Conceptualization. **Artem R. Oganov:** Writing – review & editing, Supervision, Methodology, Funding acquisition, Formal analysis, Conceptualization. **Dianzeng Jia:** Writing – review & editing, Supervision, Resources, Project administration, Methodology, Funding acquisition, Formal analysis, Conceptualization.

Declaration of competing interest

The authors declare that they have no known competing financial interests or personal relationships that could have appeared to influence the work reported in this paper.

Acknowledgments

This work was supported by the National Natural Science Foundation of China (U2003307, 22105163), the Science and technology innovation leader of Xinjiang Uygur Autonomous Region of China (2022TSYCLJ0043), the Natural Science Foundation of Xinjiang Uygur Autonomous Region of China (2021D01D09, 2021D01C097, 2022D01C701), the Open Project of Key Laboratory in Xinjiang Uygur Autonomous Region of China (2023D04032), the Excellent Doctoral Student Research Innovation Project of Xinjiang University (XJU2022BS044), and the Scientific Research Program of the Higher Education Institution of Xinjiang (XJEDU2021Y005). A. R.O. thanks the Russian Science Foundation (grant 19-72-30043).

Appendix A. Supplementary material

Supplementary data to this article can be found online at https://doi.org/10.1016/j.jechem.2026.04.058.

References

[1] L. Deng, S. Hung, S. Liu, S. Zhao, Z. Lin, C. Zhang, Y. Zhang, A. Wang, H. Chen, J. Peng, R. Ma, L. Jiao, F. Hu, L. Li, S. Peng, J. Am. Chem. Soc. 146 (2024) 23146–23157.
[2] F. Pan, C. Gong, Y. Sun, Z. Wu, D. Li, J. Wu, X. Cao, Y. Xu, X. Li, H. Gao, J. Zhang, Y. Zhao, H. Liu, J. Energy Chem. 107 (2025) 872–880.
[3] Y. Huang, Z. Wang, H. Xiao, Q. Liu, X. Wang, J. Am. Chem. Soc. 146 (2024) 29006–29016.
[4] J. Moon, W. Beker, M. Siek, J. Kim, H.S. Lee, T. Hyeon, B.A. Grzybowski, Nat. Mater. 23 (2024) 108–115.
[5] J. Cao, D. Zhang, B. Ren, P. Song, W. Xu, Energy Environ. Sci. 17 (2024) 5911–5921.
[6] W. He, X. Tan, Y. Guo, Y. Xiao, H. Cui, C. Wang, Angew. Chem. Int. Ed. 63 (2024) e202405798.
[7] M. Zha, C. Pei, Q. Wang, G. Hu, L. Feng, J. Energy Chem. 47 (2020) 166–171.
[8] C.H. Park, H. Lee, J. Choi, T.G. Yun, Y. Lim, H.B. Bae, S. Chung, Adv. Mater. 36 (2024) 2403392.
[9] Q. Huang, G.-J. Xia, B. Huang, D. Xie, J. Wang, D. Wen, D. Lin, C. Xu, L. Gao, Z. Wu, J. Wu, F. Xie, W. Guo, R. Zou, Energy Environ. Sci. 17 (2024) 5260–5272.
[10] W. Gou, S. Zhang, Y. Wang, X. Tan, L. Liao, Z. Qi, M. Xie, Y. Ma, Y. Su, Y. Qu, Energy Environ. Sci. 17 (2024) 6755–6765.
[11] Y. Xue, J. Zhao, L. Huang, Y.-R. Lu, A. Malek, G. Gao, Z. Zhuang, D. Wang, C.T. Yavuz, X. Lu, Nat. Commun. 14 (2023) 8093.
[12] J. Zhang, D. Wu, L. Cai, Y. Lu, F. Cheng, L. Shi, Q. Yi, Y. Liu, Y. Huang, J. Energy Chem. 100 (2025) 226–233.
[13] Q. Wang, Y. Gong, X. Zi, L. Gan, E. Pensa, Y. Liu, Y. Xiao, H. Li, K. Liu, J. Fu, J. Liu, A. Stefancu, C. Cai, S. Chen, S. Zhang, Y. Lu, T. Chan, C. Ma, X. Cao, E. Cortés, M. Liu, Angew. Chem. Int. Ed. 63 (2024) e202405438.
[14] T. Lin, H. Yang, J. Dong, C. Ni, X. Gao, J. Li, J. Wang, X. He, W. Tan, L. Feng, Z. Li, Fuel 396 (2025) 135282.
[15] P. Yu, X. Zhang, T. Zhang, X. Tao, Y. Yang, Y.-H. Wang, S. Zhang, F. Gao, Z. Niu, M. Fan, M. Gao, J. Am. Chem. Soc. 146 (2024) 20379–20390.
[16] Q. Wang, Q. Xie, S. Wang, L. Feng, Chem. Commun. 62 (2026) 1210–1214.
[17] P. Wang, J. Zhu, Z. Pu, R. Qin, C. Zhang, D. Chen, Q. Liu, D. Wu, W. Li, S. Liu, J. Xiao, S. Mu, Appl. Catal. B 296 (2021) 120334.
[18] Y. Wang, Y. Qin, S. Liu, Y. Zhao, L. Liu, D. Zhang, S. Zhao, J. Liu, J. Wang, Y. Liu, H. Wu, B. Jia, X. Qu, H. Li, M. Qin, J. Am. Chem. Soc. 147 (2025) 13345–13355.
[19] R. Wan, T. Yuan, L. Wang, B. Li, M. Liu, B. Zhao, Nat. Catal. 7 (2024) 1288–1304.
[20] A. Li, S. Kong, C. Guo, H. Ooka, K. Adachi, D. Hashizume, Q. Jiang, H. Han, J. Xiao, R. Nakamura, Nat. Catal. 5 (2022) 109–118.
[21] R. Ge, L. Li, J. Su, Y. Lin, Z. Tian, L. Chen, Adv. Energy Mater. 9 (2019) 1901313.
[22] N. Yu, F. Wang, X. Jiang, J. Tan, M. Hojamberdiev, H. Hu, Y.-M. Chai, B. Dong, J. Energy Chem. 102 (2025) 208–217.
[23] Y. Li, C. Li, B. Ouyang, B. Ye, S. Li, L. Zhang, T. Zhang, C. Tang, R. Chen, B. Zhang, B. Mei, X. Xia, Y. Zhang, J. Energy Chem. 117 (2026) 277–286.
[24] J. Wang, C. Cheng, Q. Yuan, H. Yang, F. Meng, Q. Zhang, L. Gu, J. Cao, L. Li, S. Haw, Q. Shao, L. Zhang, T. Cheng, F. Jiao, X. Huang, Chem 8 (2022) 1673–1687.
[25] P. Han, L. Wu, Y. Zhang, J. Yue, Y. Jin, H. Jia, W. Luo, Angew. Chem. Int. Ed. 64 (2025) e202419320.
[26] G. Xu, X. Zhou, Y. Miao, B. Jiang, Q. Sun, Z. Wu, B. Li, L. Wang, Adv. Energy Mater. 15 (2025) e03590.
[27] Y.-G. Ji, J. Wu, H. Wen, S. Wang, L. Feng, Chem. Eng. J. 496 (2024) 154211.
[28] Z. Huang, Y. Bi, J. She, Y. Liu, S. Feng, C. Xu, D. Sun, H. Liu, J. Energy Chem. 106 (2025) 619–630.
[29] J. Yang, G. Dai, W. Song, P.E.P. Win, J. Wang, X. Wang, Angew. Chem. Int. Ed. 64 (2025) e202416274.
[30] M. Jiang, J. Xu, Y. Chen, L. Wang, Q. Zhou, P. Munroe, L. Li, Z. Xie, S. Peng, Angew. Chem. Int. Ed. 64 (2025) e202424195.
[31] Z. Pei, J. Yang, J. Zhao, D. Luan, X.W. (David) Lou, Angew. Chem. Int. Ed. 65 (2026) e21873.
[32] C. Li, B. Ye, B. Ouyang, T. Zhang, T. Tang, Z. Qiu, S. Li, Y. Li, R. Chen, W. Wen, M. Song, B. Mei, X. Xia, Y. Zhang, Adv. Mater. 37 (2025) 2501381.
[33] G. Hägg, Z. Phys, Chem 12 (1931) 33.
[34] L. Dai, F. Yao, L. Yu, C. Fang, J. Li, L. Xue, S. Zhang, P. Xiong, Y. Fu, J. Sun, J. Zhu, Adv. Energy Mater. 12 (2022) 2200974.
[35] C. Yue, X.-J. Weng, G. Gao, A.R. Oganov, X. Dong, X. Shao, X. Wang, J. Sun, B. Xu, H.-T. Wang, X.-F. Zhou, Y. Tian, Fundam. Res. 1 (2021) 482–487.
[36] P. Chen, K. Xu, Z. Fang, Y. Tong, J. Wu, X. Lu, X. Peng, H. Ding, C. Wu, Y. Xie, Angew. Chem. Int. Ed. 54 (2015) 14710–14714.
[37] X. Zhu, T. Jin, C. Tian, C. Lu, X. Liu, M. Zeng, X. Zhuang, S. Yang, L. He, H. Liu, S. Dai, Adv. Mater. 29 (2017) 1704091.
[38] Z. Zhu, Y. Wang, X. Duan, P. Wang, S. Zhong, S. Ren, X. Xu, B. Gao, J. (Pimm) Vongsvivut, S. Wang, Adv. Mater. 36 (2024) 2401454.
[39] J. Han, H. Wang, Y. Wang, H. Zhang, J. Li, Y. Xia, J. Zhou, Z. Wang, M. Luo, Y. Wang, N. Wang, E. Cortés, Z. Wang, A. Vomiero, Z. Huang, H. Ren, X. Yuan, S. Chen, D. Feng, X. Sun, Y. Liu, H. Liang, Angew. Chem. Int. Ed. 63 (2024) e202405839.
[40] Z. Du, Z. Meng, X. Gong, Z. Hao, X. Li, H. Sun, X. Hu, S. Yu, H. Tian, Angew. Chem. Int. Ed. 63 (2024) e202317022.
[41] Z. Liang, D. Shen, Y. Wei, F. Sun, Y. Xie, L. Wang, H. Fu, Adv. Mater. 36 (2024) 2408634.
[42] A. Grimaud, O. Diaz-Morales, B. Han, W.T. Hong, Y.-L. Lee, L. Giordano, K.A. Stoerzinger, M.T.M. Koper, Y. Shao-Horn, Nat. Chem. 9 (2017) 457–465.
[43] Q. Jiang, S. Wang, C. Zhang, Z. Sheng, H. Zhang, R. Feng, Y. Ni, X. Tang, Y. Gu, X. Zhou, S. Lee, D. Zhang, F. Song, Nat. Commun. 14 (2023) 6826.
[44] C. Wang, P. Zhai, M. Xia, Y. Wu, B. Zhang, Z. Li, L. Ran, J. Gao, X. Zhang, Z. Fan, L. Sun, J. Hou, Angew. Chem. Int. Ed. 60 (2021) 27126–27134.
[45] H.B. Tao, Y. Xu, X. Huang, J. Chen, L. Pei, J. Zhang, J.G. Chen, B. Liu, Joule 3 (2019) 1498–1509.
[46] Y. Mei, Y. Feng, C. Zhang, Y. Zhang, Q. Qi, J. Hu, ACS Catal. 12 (2022) 10808–10817.
[47] Y. Wen, P. Chen, L. Wang, S. Li, Z. Wang, J. Abed, X. Mao, Y. Min, C.T. Dinh, P.D. Luna, R. Huang, L. Zhang, L. Wang, L. Wang, R.J. Nielsen, H. Li, T. Zhuang, C. Ke, O. Voznyy, Y. Hu, Y. Li, W.A. Goddard III, B. Zhang, H. Peng, E.H. Sargent, J. Am. Chem. Soc. 143 (2021) 6482–6490.
[48] Z. Shi, Y. Wang, J. Li, X. Wang, Y. Wang, Y. Li, W. Xu, Z. Jiang, C. Liu, W. Xing, J. Ge, Joule 5 (2021) 2164–2176.
[49] Y. Wu, Y. Zhao, P. Zhai, C. Wang, J. Gao, L. Sun, J. Hou, Adv. Mater. 34 (2022) 2202523.
[50] E. Jiang, C. Guo, X. Zhao, Y. Chao, D. Ma, P. Huo, Y. Yan, P. Zhou, Y. Yan, ACS Nano 17 (2023) 10774–10782.
[51] Y. Hao, S.-F. Hung, W.-J. Zeng, Y. Wang, C. Zhang, C.-H. Kuo, L. Wang, S. Zhao, Y. Zhang, H.-Y. Chen, S. Peng, J. Am. Chem. Soc. 145 (2023) 23659–23669.
[52] X. Luo, H. Zhao, X. Tan, S. Lin, K. Yu, X. Mu, Z. Tao, P. Ji, S. Mu, Nat. Commun. 15 (2024) 8293.
[53] H. Liu, D. Zhang, S.M. Holmes, C. D'Agostino, H. Li, Chem. Sci. 14 (2023) 9000–9009.
[54] C.-T. He, L.-H. Yu, H. Liu, Q. Wang, Z.-M. Ye, J. Zhang, L.-D. Wang, M.-Q. He, X.-F. Zhang, H.-G. Du, Z.-W. Lu, J. Yang, H.-H. Huang, X.-M. Chen, Nat. Commun. 16 (2025) 4389.
[55] R. Zhang, L. Pan, B. Guo, Z.-F. Huang, Z. Chen, L. Wang, X. Zhang, Z. Guo, W. Xu, K.P. Loh, J.-J. Zou, J. Am. Chem. Soc. 145 (2023) 2271–2281.
[56] E. Santos, W. Schmickler, ChemPhysChem 7 (2006) 2282–2285.

Jingmei Min is currently pursuing her Ph.D. degree under the supervision of Prof. Jixi Guo and Dianzeng Jia at the College of Chemistry of Xinjiang University. Her current research focuses on the design and synthesis of transition metal-based materials for electrocatalysis.

Jixi Guo is currently a full Professor at the College of Chemistry of Xinjiang University. He received his bachelor's degree from Shandong University in 2004, and his master's and Ph.D. degrees from Xinjiang University in 2008 and 2012, respectively. He then conducted postdoctoral research at Chinese University of Hong Kong (CUHK). His current research focuses on catalytic materials and carbon-based functional materials.

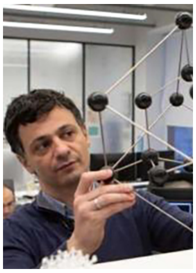

Artem R. Oganov is a Distinguished Professor at the Skolkovo Institute of Science and Technology (Skoltech) and, since 2026, Chief Science Officer at SberUniversity. He graduated with a summa cum laude in Crystallography from Moscow State University in 1997, received his Ph.D. from University College London in 2002, and his Habilitation from ETH Zurich in 2007. He created USPEX, a breaktgrough evolutionary algorithm for crystal structure prediction used worldwide. His work spans computational materials discovery, high pressure chemistry, and mineral physics. Among his top distinctions: Highly Cited Researcher (2022, 2024, 2025), Fellow of the Royal Society of Chemistry and the American Physical Society, Professor of the Russian Academy of Sciences, and member of Academia Europaea.

Dianzeng Jia is currently a full Professor and the Director of the State Key Laboratory of Chemistry and Utilization of Carbon Based Energy Resources at Xinjiang University. He received his bachelor's degree from Xinjiang University in 1983 and his master's degree from Nanjing University in 1992. In 2005, he obtained his Ph.D. degree from Sichuan University. His current research focuses on the synthesis and applications of nanocomposites and carbon materials.